Journal of Cluster Science
https://doi.org/10.1007/s10876-018-1348-8

ORIGINAL PAPER

Understanding the "Activation" of the Nanocluster $[H_xPMo_{12}O_{40}\subset H_4Mo_{72}Fe_{30}(O_2CMe)_{15}O_{254}(H_2O)_{98-y}(EtOH)_y]$ for Low Temperature Growth of Carbon Nanotubes

Gibran L. Esquenazi[1] · Andrew R. Barron[1,2,3]

Received: 19 December 2017

Abstract
The molecular nanocluster $H_xPMo_{12}O_{40}\subset H_4Mo_{72}Fe_{30}(O_2CMe)_{15}O_{254}(H_2O)_{98-y}(EtOH)_y$ (FeMoC), was the first molecular catalyst precursor (pro-catalyst) that promised controlled growth of carbon nanotubes (CNTs); however, temperatures in excess of ~ 900 °C or the addition of excess iron were required as catalyst promoters for CNT growth. To understand these disappointing results the "activation" of FeMoC for CNT growth was studied by systematic investigation of H_2 gas concentration and growth temperature. The pathway for "activation" of FeMoC occurs through the sufficient reduction of both metal oxide components in the pro-catalyst. By ensuring pro-catalyst reduction prior to introduction of growth gases, we demonstrate for the first time, growth of CNTs at temperatures as low as 600 °C without the use of catalyst promoters using the single molecular precursor, FeMoC. To understand the role of catalyst promoters used in prior work, thermogravimetric analysis experiments were performed. The addition of an iron catalyst promoter is observed to play two key roles in the "activation" of FeMoC: (1) to replenish sublimated metal atoms, and (2) to reduce the reduction temperature required for reduction of FeMoC into an "active" catalyst. These results caution the conditions employed in many earlier studies for CNT growth, and create new possibilities for molecular pro-catalysts.

Keywords Activation · Catalyst · Carbon nanotube (CNT) · Polyoxometalate (POM)

Introduction

Carbon nanotubes (CNTs) exhibit superlative properties that vary strongly with their diameter and chirality [1–3]. In order to utilize their structure-dependent properties controlled growth of selected diameters and chiralities is desired. Current CVD growth generally produces a mixture of diameters and chiralities unsuitable for applications, such as electronics, that require defined structures. However, limited control over CNT morphology has been reported by tuning CVD growth conditions, such as gaseous composition, substrate, and growth temperature [4–6]. Of particular interest are the reports of narrowed chirality and diameter distributions at lower growth temperatures [6, 7]. Lowering growth temperature is an attractive approach given the distinct economic impact on commercialization and desire for compatible processing in electronics. Lowering growth temperature may also circumvent problems associated with high-temperature CNT synthesis, such as Ostwald ripening and catalyst migration, which in theory would provide enhanced control over diameter distributions, and possibly, chirality as well.

Traditionally, the most common route to achieve high chiral selectivity is through control of catalyst size due to the reported correlation between catalyst size and resulting nanotube diameter [8–10]. For catalyst of similar size, we have previously shown the chemical composition $M^1_xM^2_y$ of binary metal oxide nanoparticles has a significant control over the range of chiralities grown [11]. Therefore a

Electronic supplementary material The online version of this article (https://doi.org/10.1007/s10876-018-1348-8) contains supplementary material, which is available to authorized users.

✉ Andrew R. Barron
arb@rice.edu

[1] Department of Chemistry, Rice University, Houston, TX 77005, USA

[2] Department of Materials Science and Nanoengineering, Rice University, Houston, TX 77005, USA

[3] Energy Research Safety Institute (ESRI), Swansea University, Bay Campus, Swansea SA1 8EN, Wales, UK

Published online: 17 February 2018

Table 1 Summary of prior work with FeMoC

Catalyst	Growth Temperature (°C)	CNT growth observations	Reference
FeMoC + promoter[a]	900	CNT growth	16
FeMoC[b]	700, 800	No growth	17
FeMoC[b]	900	Minimal	17
FeMoC-Pyz-$Fe(NO_3)_3$[c]	900	CNT growth	17
FeMoC	900	Minimal	18
FeMoC	950, 1000	CNT growth	18
FeMoC	880	CNT growth	19
FeMoC	1010	Minimal	20
FeMoC	900	Minimal	21
FeMoC	920, 940, 970	CNT growth	21

[a]Additional iron powder catalyst used

[b]Purified FeMoC coordinated with EtOH. cPyrazine functionalized FeMoC reacted with $Fe(NO_3)_3$

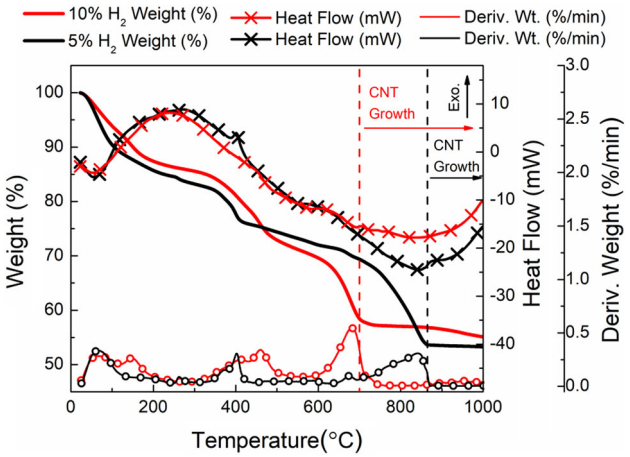

Fig. 1 The TGA/DSC for 5% (red) and 10% (black) hydrogen reduction of FeMoC. The weight (%) is depicted as solid lines. The heat flow (mW) lines are marked with the symbol "X", and the exothermic direction is up. The derivative weight (%/min) lines are marked with the "O" symbol

possible route to chiral-selective growth is through the use of catalysts with controlled sizes and compositions under optimized CVD conditions. Considering the problems in controlling the composition and size of binary metal oxide nanoparticles [12] single molecular precursors would be considered an ideal solution: given the unique composition and hence size of the final nanoparticle. Recently, Li et al. used the molecular nanocluster $Na_{15}[Na_3 \subset \{Co(H_2O)_4\}_6 \{WO(H_2O)\}_3(P_2W_{12}O_{48})_3] \cdot nH_2O$ to selectively grow (12,6), (14,4), and (16,0) CNTs in efficiencies of 92, 97, and 80% respectively [13–15]. They propose the high chiral selectivity arises from two key factors: 1) the excellent matching between the (n,m) nanotube chirality and the Miller (plane) indices of the μ-phase W_6Co_7 alloy, and 2) the stability of the high melting point alloy that maintains its well-defined structure under CVD conditions.

The first report of a molecular precursor for the growth of CNTs was by Liu and co-workers [16] who showed that single walled carbon nanotubes (SWCNTs) may be grown using the molecular nanocluster $[H_xPMo_{12}O_{40} \subset H_4Mo_{72}Fe_{30}(O_2CMe)_{15}O_{254}(H_2O)_{98}]$ (FeMoC). This compound is a single molecular nanocluster similar to the W-Co nanocluster used by Li et al. [13–15] They both represent potential precursors for high-temperature μ-phase alloys (Mo_6Fe_7 versus W_6Co_7). However, despite being set-up as an ideal precursor, it was found necessary to add a catalyst promoter (an external source of metal) to FeMoC to enable growth of CNTs, and then at only elevated temperatures (900 °C, see Table 1). We subsequently found that even with ligand exchange (EtOH for H_2O) and purification, the nanocluster on its own resulted in essentially no observable growth at ≤ 900 °C [17]. As with the report by Liu, we found that additional Fe is required in order to achieve SWNT growth at 900 °C. Later, Edgar et al. [18], Jeon et al. [19], Goss et al. [20], Peng et al. [21], demonstrated CNT growth by employing growth temperatures in the range of 880-1010 °C without the use of additional catalyst promoters. The excessive growth temperatures required with FeMoC appear to counter previous work with Fe-Mo catalyst systems demonstrating CNT growth at temperatures as low as 550 °C [22–24]. It should be noted that both Fe and Mo have been shown to be efficient catalysts both independently and as mixed metal nanoparticles [25–30]; thus, FeMoC should be "active" for CNT growth, but under the prior growth conditions studied it is not [16–21].

In the intervening years a great deal more has been learnt about the differences between the conditions (temperature and source gas composition) for nucleation versus growth of CNTs [31, 32]. We are therefore interested in determining what the threshold for catalytic activity is, and why FeMoC appeared not to work as expected, despite being the original molecular pro-catalyst precursor. This

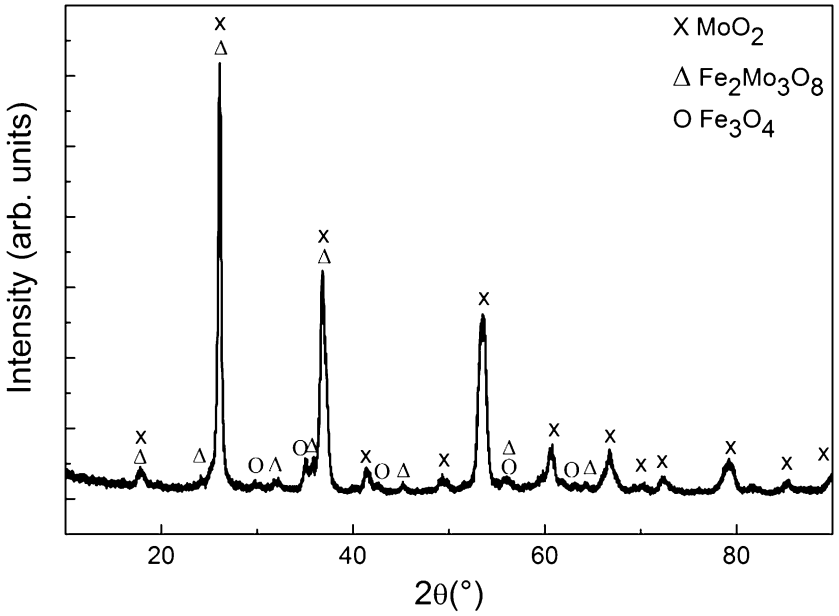

Fig. 2 The XRD pattern for FeMoC after reduction at 500 °C in 10% H_2 atmosphere. The MoO_2 reflection is marked with the "X" symbol (ICDD 04-013-3645). The $Fe_2Mo_3O_8$ reflection is marked with the "Δ" symbol (ICDD 00-036-0526). The Fe_3O_4 reflection is marked with the "O" symbol (ICDD 01-080-6410)

paper aims to address these questions, and to evaluate new conditions that enable low-temperature growth of CNTs. This systematic study of hydrogen gas concentration and growth temperature reveals the importance of CVD pretreatment of FeMoC in its "activation" for CNT growth. By ensuring sufficient reduction of the metal oxide components in FeMoC, we demonstrate growth of CNTs at temperatures as low as 600 °C without the use of additional catalyst promoters. This paper also elucidates the role of catalyst promoters utilized for CNT growth observed in prior work with FeMoC.

Experimental

Materials

Chemicals for the synthesis of FeMoC (phosphomolybdic acid hydrate, sodium molybdate dihydrate, and iron(II) chloride tetrahydrate), iron oxide nanoparticles (iron(III) acetylacetonate, oleic acid, 1-2-hexadecanediol, benzyl phenyl ether), molybdenum nanoparticles (molybdenum hexacarbonyl), catalyst promoter (iron(III) chloride), and ethanol (200 proof) was purchased from Sigma Aldrich and used as received. The 5 and 10% hydrogen gas (Ar balance) were obtained from Matheson Tri-Gas. Spin-on-glass (SOG) precursor IC1-200 was obtained from Futtrex, Inc.

Preparation of Nanoparticles

FeMoC was synthesized and purified as previously reported [17]. Magnetite nanoparticles were synthesized using a thermal decomposition reaction reported by Sun and co-

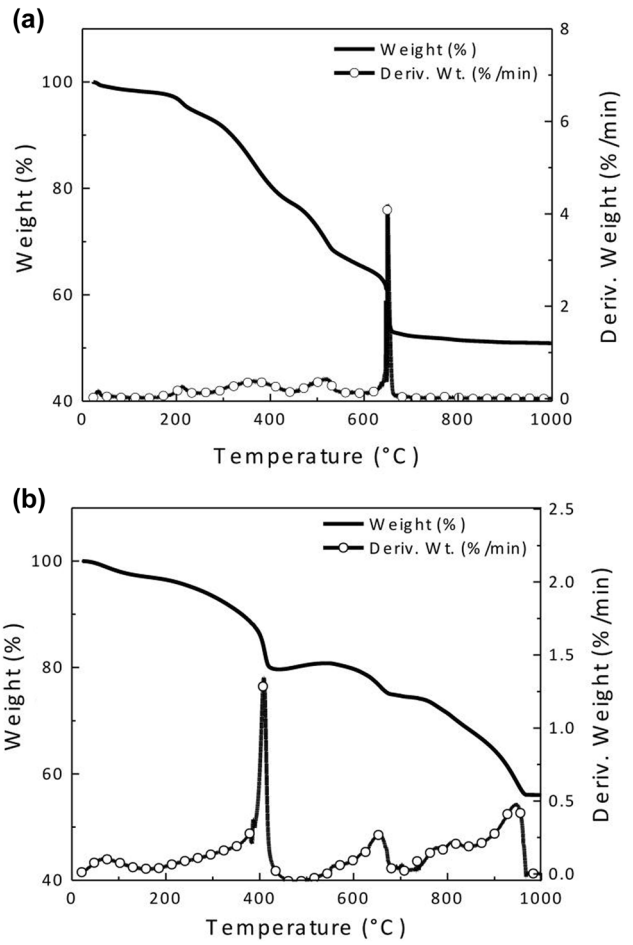

Fig. 3 The TGA profiles in 10% H_2 atmosphere for Fe_3O_4 nanoparticles (**a**) and MoO_3 nanoparticles (**b**). Weight% is depicted as solid lines, while the dTGA (Deriv. Weight%/min) is marked with the symbol "O"

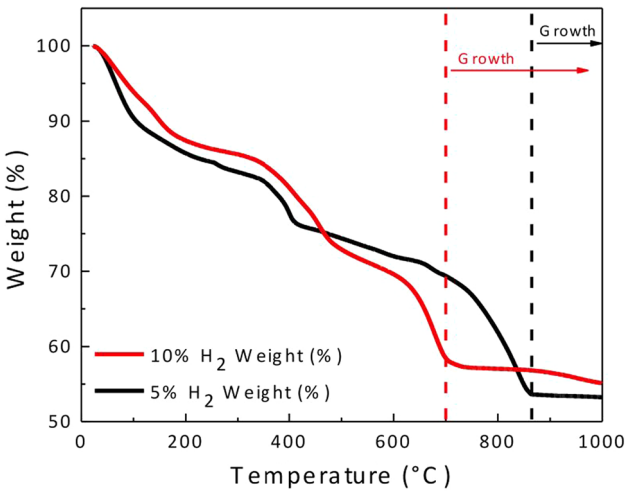

Fig. 4 CNT growth expectations derived from TGA results. For 5% hydrogen (black), CNT growth is expected for temperatures > 800 °C. For 10% hydrogen (red), CNT growth is expected at temperatures > 700 °C

workers [33]. Molybdenum nanoparticles were prepared using a modified thermal decomposition reaction reported by Park et al. [34] Here, 2.0 g of molybdenum hexa carbonyl was added to 50 mL of benzyl phenyl ether in a 100-mL three-neck flask. Then 1 mL of oleic acid and a stir bar was added to the flask. A cold condenser was attached to prevent complete sublimation of MoO_3. The mixture was then heated slowly to 310 °C and held for 30 min while stirring. Air was then bubbled into the hot mixture for 30 min. The resulting mixture was then cooled to room temperature before adding 50 mL of EtOH. The nanoparticles were centrifuged and washed three times with EtOH before being left to air dry.

CNT Growth

The synthesis of CNTs was carried out using a Nanotech innovations SSP-354 two-zone liquid injection furnace [35]. The carrier gas used was either 5 or 10% hydrogen gas (argon balance). Substrates were spin-on-glass (SOG) prepared by spin coating IC1-200 intermediate coating (Futtrex, Inc.) on SiN_x coated Si wafers followed by annealing in air at 600 °C. A 50 µL of FeMoC solution (0.1 µM concentration in EtOH) was then spin coated onto the substrate. The substrates were then immediately placed into the two-zone furnace. The second zone (the reaction zone) of the furnace was set to 200 °C and the samples were allowed to anneal in air for 10 min. Afterwards, the H_2/Ar composite gas was turned on (1 L/min) and the first zone of the furnace was set to 225 °C. The second zone was then set to the growth temperature (700, 800, and 900 °C), followed by a 15 min dwell. Afterwards, a 3 mL EtOH solution was injected at a constant injection speed of 1 mL/h. Upon injection completion, the furnace was turned off and cooled under H_2/Ar atmosphere. For multi-step CNT synthesis, a 15 min dwell at 925 °C was conducted

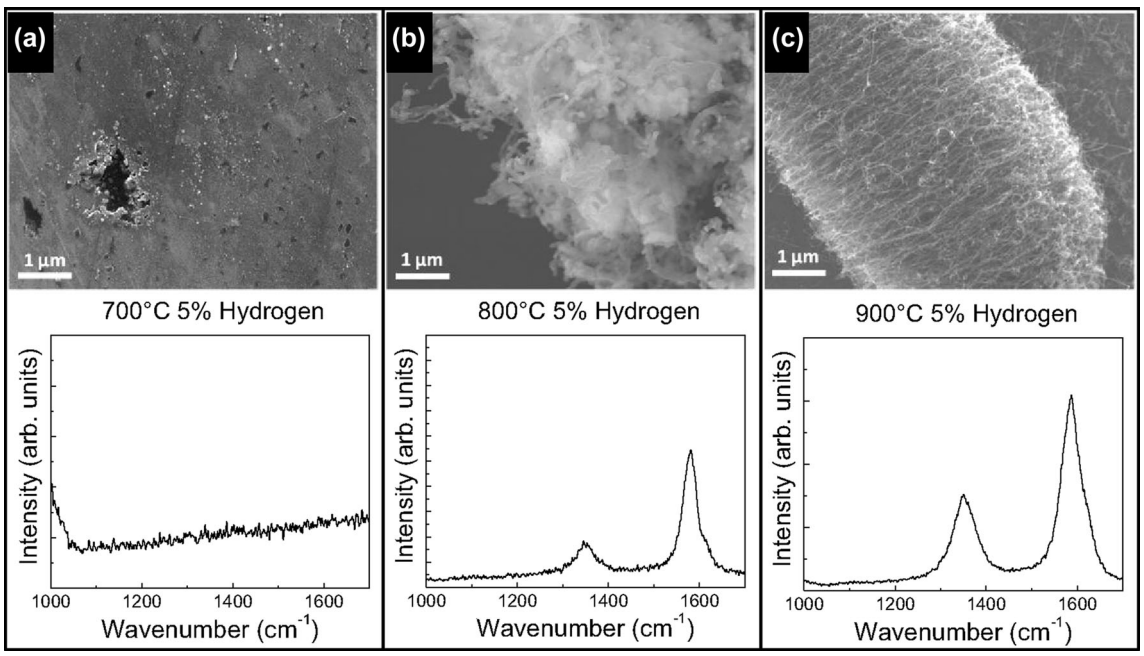

Fig. 5 SEM images and corresponding Raman spectra (514.5 nm) for CNT growth experiments conducted in 5% hydrogen at growth temperatures of **a** 700 °C, **b** 800 °C, and **c** 900 °C

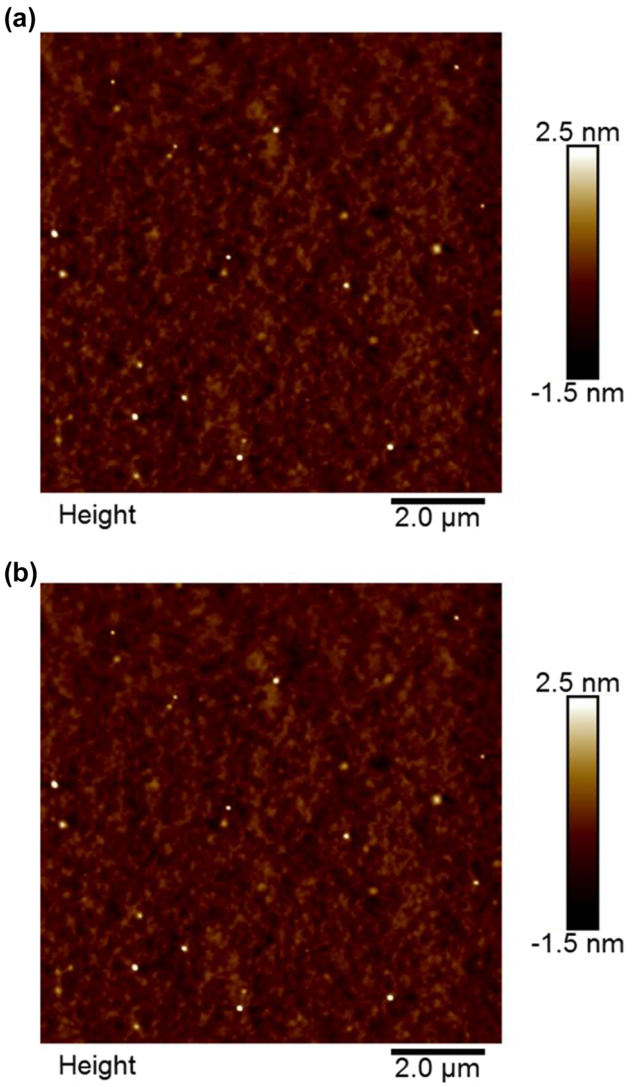

Fig. 6 The AFM images of FeMoC (0.1 μM conc.) spin coated on SOG substrates before (**a**) and after heat treated with a 15 min dwell at 925 °C in a 5% hydrogen environment (**b**)

before the furnace temperature was reduced to the growth temperature (600, 700, and 800 °C).

Characterization

Simultaneous thermogravimetric analysis/differential scanning calorimetry (TGA/DSC) experiments were performed on a TA instruments Q-600 using 5 and 10% H_2 (Ar balance) blends as a carrier gas. A sample of concentrated FeMoC-EtOH solution (1 mL) was allowed to evaporate resulting in solid FeMoC samples (20 mg). The samples were then placed in alumina pans and heated with a ramp rate of 3.00 °C/min under a 70 mL/min flow of the carrier gas. X-ray diffraction (XRD) measurements were performed on a Rigaku D/Max Ultima II using a Cu-Kα radiation source operating at 40 kV and 40 mA. The XRD patterns were analyzed using Rigaku's PDXL2 software (Version 2.4.2.0). SEM was performed on a JEOL 6500F by placing samples on double-sided carbon tape that is fixed to aluminum SEM stubs, used as received. Images were acquired with a typical operating voltage of 15 kV, with a working distance of 10 mm, and spot size of 3. Raman spectra were obtained using a Renishaw inVia Raman Microscope, at 514.5 nm wavelength, using a 50 × LWD lens, data was acquired with 5 or more accumulations between 100 and 3300 cm^{-1} with cosmic-ray background removal applied. AFM measurements were taken on a Bruker MultiMode 8 system in ScanAsyst™ mode. A ScanAsyst-Air tip with a drive frequency of 70 kHZ was used. Images were taken at a scan frequency of 1 Hz and 512 samples/line. Samples were prepared by taking an aliquot of the FeMoC solution and diluting to a final concentration of 0.1 μM in EtOH. One drop of the solution was spin coated onto a SOG wafer at 3000 rpm for 40 s and dried in air before imaging. AFM analysis was performed using the NanoScope Software (Version 1.5.0.0) provided by Bruker. X-ray photoelectron spectroscopy (XPS) measurements were obtained using a PHI Quantera system with an aluminum X-ray source at 1486.7 eV. A spectrum energy calibration was performed with respect to the C 1*s* peak with binding energy set to 284.50 eV (NIST XPS database). The speciation and composition variation was obtained by recording the multiplex spectra for C 1*s*, O 1*s*, Fe 2*p* and Mo 3*d* elemental energy levels. Data was collected using multi-cycle scans with a pass energy of 26 eV. Data was analyzed with PHI MultiPak program (Version 9.6.1.7). The UV–visible measurements were performed on an Agilent 8453 instrument. The spectrum of the EtOH diluted FeMoC solution displayed the characteristic bands at 550, 880, and 1045 nm corresponding to the nucleus shell charge transfer between Keggin guest and host (550 nm) and the [Mo(V) → Mo(VI)] charge transfer in the Keggin cluster (880 and 1045 nm) as previously reported [17].

Results and Discussion

Thermogravimetric Analysis of FeMoC and Fe-Mo oxides

As depicted in Table 1 FeMoC appears to only be "active" for CNT growth above 900 °C. To understand this, we have investigated the thermal behavior of FeMoC using simultaneous thermogravimetric and differential scanning calorimetry (TGA/DSC) analysis. Figure 1 shows the TGA/DSC of FeMoC under a H_2/Ar atmosphere with 5 and 10% H_2. Under either atmosphere the initial mass loss

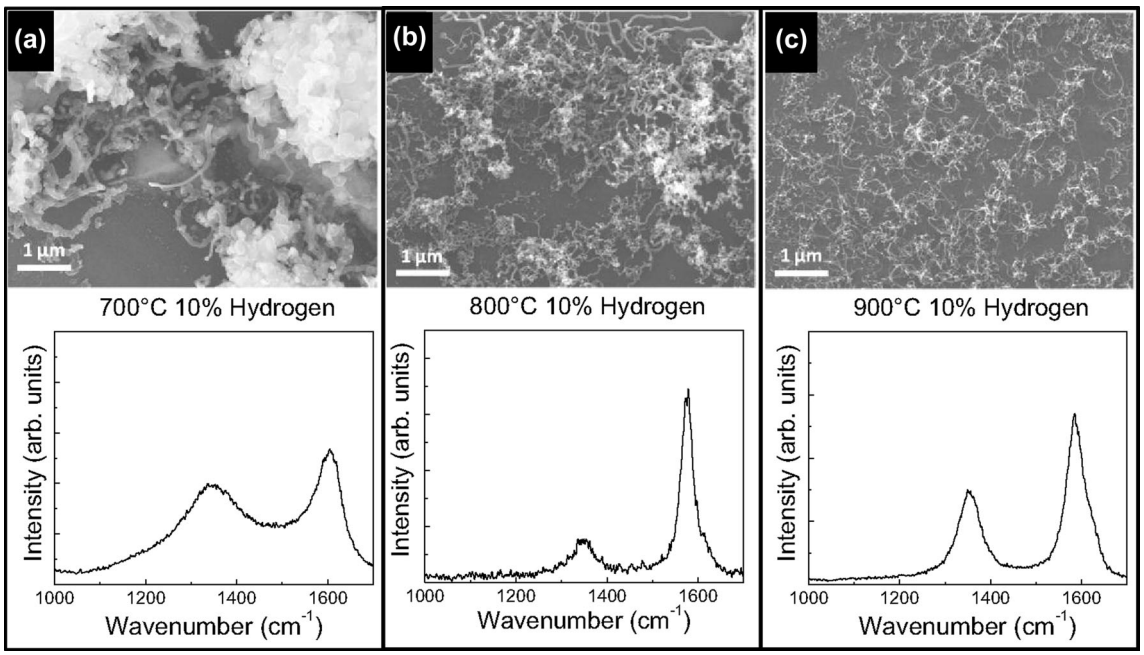

Fig. 7 SEM images and corresponding Raman spectra (514.5 nm) for CNT growth experiments conducted in 10% hydrogen at growth temperatures of **a** 700 °C, **b** 800 °C, and **c** 900 °C

Table 2 Summary of characterization results for CNT growth experiments for 5 and 10% hydrogen

Growth temperature (°C)	H_2 (%)	TGA expectation[a]	SEM observations	Raman observations
700	5	No CNTs	No CNTs	No CNTs
700	10	Minimal	Minimal CNTs	CNT[b]
800	5	No CNTs	Minimal CNTs	CNT[b]
800	10	CNT growth	CNT growth	CNT[b]
900	5	CNT growth	CNT growth	CNT[b]
900	10	CNT growth	CNT growth	CNT[b]

[a]Expected CNT growth derived from the TGA results shown in Fig. 4. [b] Observation of G ($\sim$ 1580 cm^{-1}) and D peaks ($\sim$ 1350 cm^{-1}) in the Raman spectra

occurs below 200 °C and is associated with the loss of H_2O and EtOH constituents as evidenced by the endothermic peak. Below approximately 400 °C there is a broad exothermic peak corresponding to the decomposition of the organic substituents. This measured weight loss (exptl. $\sim$ 85%, calc. $\sim$ 83%) is consistent with the loss of all water and organic substituents. The continued reduction of FeMoC reveals two additional weight loss peaks attributed to the reduction of the Fe-Mo oxide components as corroborated by the endothermic profile. It is evident that the last peak is very dependent on the composition of the carrier gas. At low H_2 concentration the observed dTGA peak (Derive. Weight %/min) is at $\sim$ 840 °C. In contrast, with 10% hydrogen the dTGA peak is significantly reduced to $\sim$ 680 °C.

To clarify the middle mass loss (350 °C < T < 650 °C) XRD characterization was undertaken after TGA/DSC reduction of FeMoC at 500 °C in 10% hydrogen. The XRD pattern shows reflections for MoO_2, Fe_3O_4, and $Fe_2Mo_3O_8$ phases (Fig. 2). The presence of $Fe_2Mo_3O_8$ is of particular interest given prior work by Yoshida et al. [36] demonstrating that the formation of inactive iron-molybdenum oxides, such as $Fe_2Mo_3O_8$, and $Fe_{3-x}Mo_xO_4$, are detrimental for CNT growth. To further elucidate the reduction of FeMoC, TGA was conducted on Fe_3O_4 and MoO_3 nanoparticles. As seen in Fig. 3a, the complete reduction Fe_3O_4 to Fe^0 is observed at $\sim$ 670 °C. While for MoO_3 nanoparticles the reduction to Mo^0 is not completed until temperatures in excess of $\sim$ 950 °C (Fig. 3b). These results suggest that the poor catalytic activity previously reported with FeMoC at low temperatures is likely caused by the adverse effects of the residual oxides, i.e., the formation of $Fe_2Mo_3O_8$ and incomplete reduction of MoO_3. The observed CNT "activation" at high temperatures was likely a result of completely reducing the pro-catalyst FeMoC to an active phase. It follows that if complete

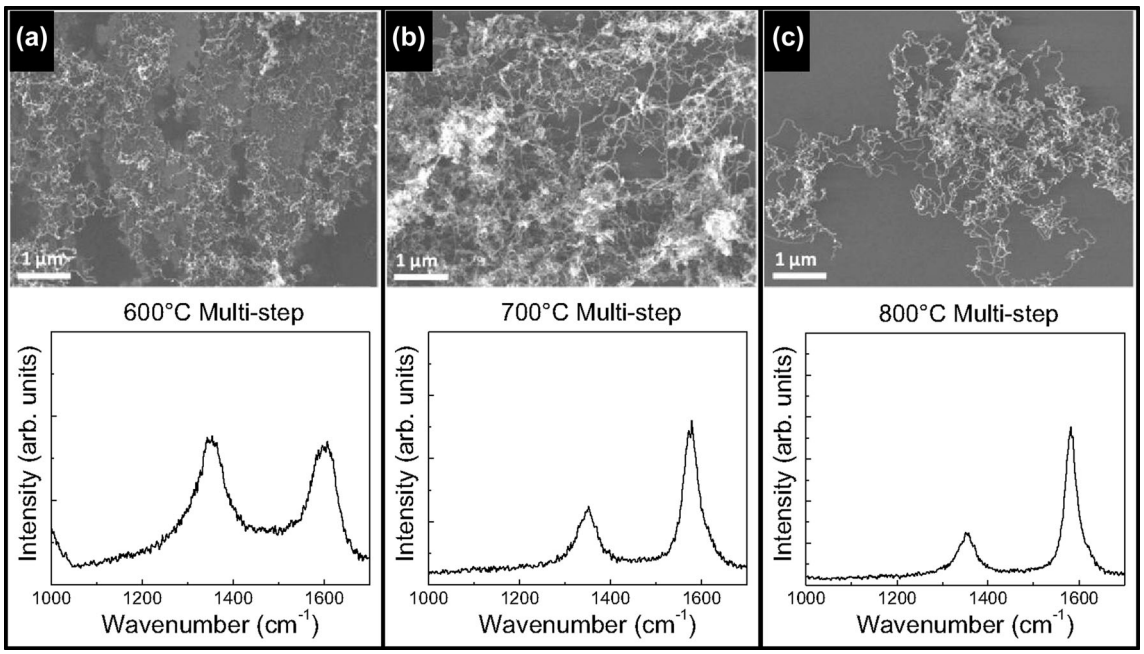

Fig. 8 SEM images and corresponding Raman spectra (514.5 nm) for CNT multi-step growth experiments conducted in 5% hydrogen at growth temperatures of **a** 600 °C, **b** 700 °C, and **c** 800 °C

reduction is necessary for "activation" of FeMoC we should expect CNT growth to correspond with temperature and hydrogen concentration as seen in Fig. 4.

CNT Growth Experiments

To investigate this further, CNT growth experiments were conducted at growth temperatures of 700, 800, and 900 °C under both 5 and 10% hydrogen atmospheres. The results under 5% hydrogen atmosphere are shown in Fig. 5. At 700 °C (Fig. 5a) no evidence of CNT growth was found by SEM or Raman spectroscopy. SEM imaging at 800 °C shows minimal growth defined here by less than 20 CNTs shown in a 100 μm^2 area. The results at 800 °C do show a Raman spectra with a pronounced G ($\sim$ 1580 cm^{-1}) and D peaks ($\sim$ 1350 cm^{-1}), characteristic of CNTs (Fig. 5b) [37]. For growth at 900 °C, the SEM images show very dense CNT growth with a tangled morphology. The Raman spectra also shows the D ($\sim$ 1350 cm^{-1}) and G peaks ($\sim$ 1580 cm^{-1}) (Fig. 5c). Analysis of the radial breathing mode (RBM) of the Raman spectra, and AFM measurements provide no evidence for SWCNTs under the conditions tested indicating that the CNT growth consisted of multi-walled carbon nanotubes (MWCNTs). The presence of MWCNTs could be due to catalyst coarsening [38, 39]. To determine if catalyst coarsening is occurring before introduction of growth gasses AFM studies were conducted. The AFM images in Fig. 6 compare the same FeMoC sample before and after a 15 min dwell at 925 °C under a 5% hydrogen atmosphere. The AFM images provided no evidence of catalyst coarsening prior to injection of carbon precursor, in agreement with prior work with FeMoC [17, 21]. This suggests that catalyst coarsening is occurring during CNT growth. It should be noted that prior work with FeMoC mainly demonstrated growth of SWCNTs. Nevertheless, these results confirm the proposal that complete reduction of the FeMoC is required for CNT growth.

The results of CNT growth under 10% hydrogen atmosphere are shown in Fig. 7 and confirm the predicted from Fig. 4. At 700 °C (Fig. 7a) the SEM and Raman results indicate minimal MWCNT growth. SEM images reveal the sparse growth of CNTs with a curly morphology, and the Raman spectra reveals the G and D peaks. At 800 °C (Fig. 7b) MWCNT growth is observed. SEM shows dense growth of tangled MWCNTs corroborated by the corresponding Raman spectra. At 900 °C (Fig. 7c) it is evident that FeMoC is active for CNT growth. SEM shows MWCNTs with a curly morphology, and the Raman spectra depicts the MWCNT characteristic D and G peaks.

The results from both 5 and 10% hydrogen atmospheres are in good agreement with expectations derived from the TGA results as shown in Table 2. These results suggest that the mechanism for "activation" of the pro-catalyst FeMoC is due to the sufficient reduction of the iron-molybdenum oxide components. Sufficient reduction likely prevents the formation of Fe-Mo oxide species that are detrimental to CNT growth, such as $Fe_2Mo_3O_8$ and $Fe_{3-x}Mo_xO_4$, therefore enabling the pro-catalyst FeMoC to become "active" in CNT growth.

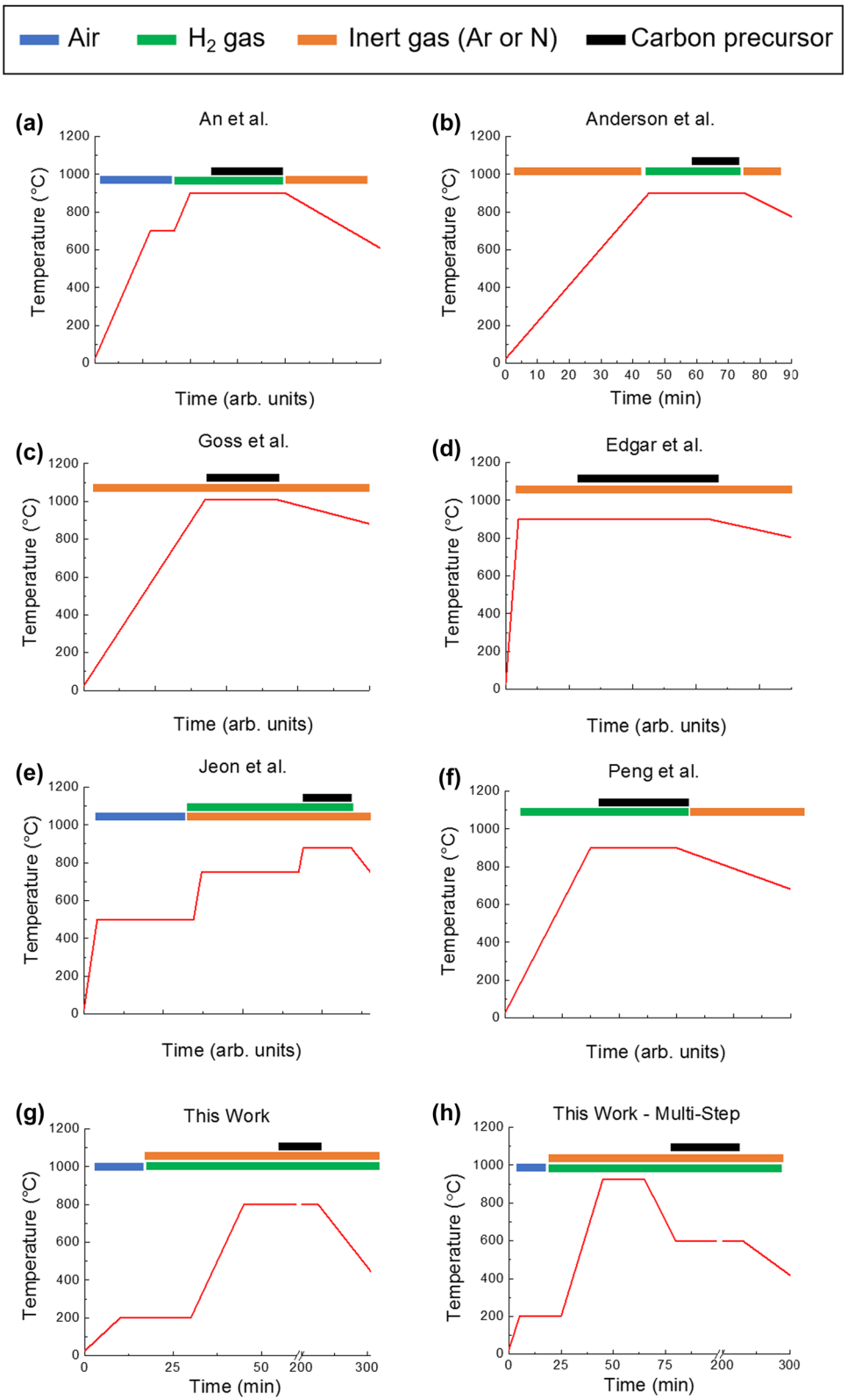

Fig. 9 The approximate CVD heating profile and conditions employed by **a** An et al. [16], **b** Anderson et al. [17], **c** Edgar et al. [18], **d** Peng et al. [21], and **e**, **f** this work. The CVD temperature profile is depicted by the red line, and the CVD conditions for air (blue), H_2 gas (green), inert gas (orange), and carbon precursor (black) are also depicted (Color figure online)

By ensuring reduction prior to the introduction of growth gases it should therefore be possible to grow CNTs at lower temperatures. To investigate this further, CNT growth experiments were conducted after a 15 min dwell at 925 °C under 5% H_2 prior to introduction of EtOH at growth temperatures of 600, 700, and 800 °C. The results from this new multi-step catalyst pre-treatment are shown in Fig. 8, and clearly show MWCNT growth at all growth

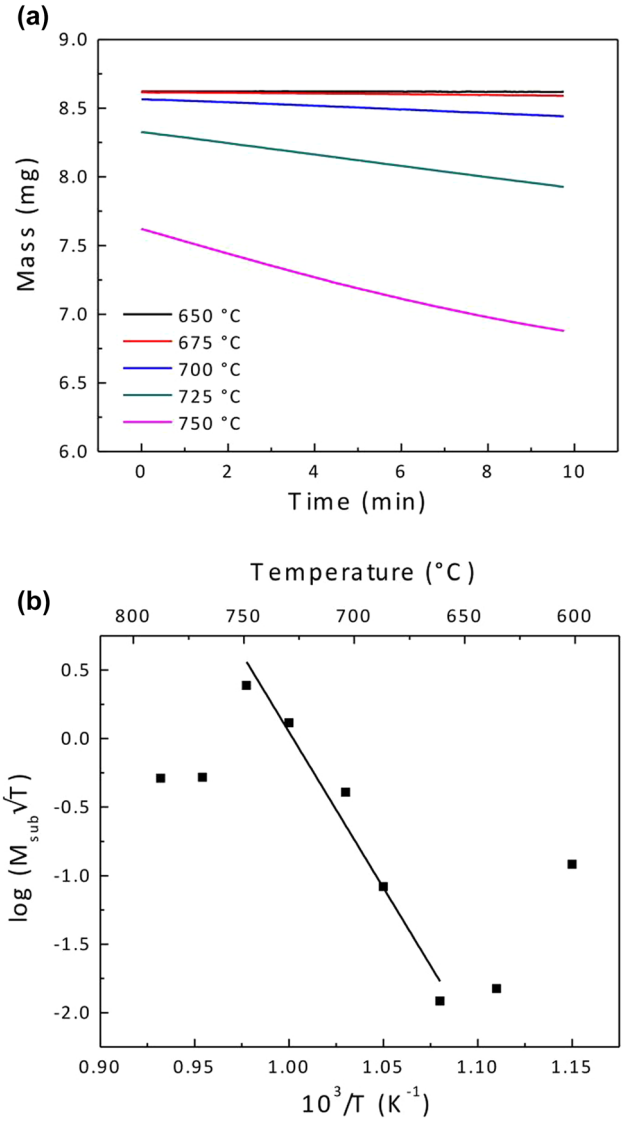

Fig. 10 The mass loss measured by isothermal TGA at different temperatures **a** and **b** the plot of $\log(M_{sub}\sqrt{T})$ versus 1/T and the determination of ΔH_{sub} (421.9 kJ/mol) for FeMoC, ($R^2 = 0.9752$)

temperatures tested. At all temperatures SEM imaging shows MWCNTs with a curly morphology (Fig. 8). The Raman spectra for the temperatures tested show the characteristic D and G peaks indicative of MWCNTs. By ensuring sufficient pro-catalyst reduction prior to introduction of growth gasses, we have shown for the first time that FeMoC can be "activated" for CNT growth at temperatures as low as 600 °C without the aid of catalyst promoters.

Evaluating Pro-catalyst Pre-treatment

The pre-treatment of the pro-catalyst FeMoC into an "active" phase is crucial for CNT growth. In typical CVD processes, catalyst pre-treatment consists of two steps, catalyst calcination and reduction. In the calcination step, the catalyst is heat treated in air or an inert gas to stabilize the catalysts prior to reduction [40]. Therefore, to better understand the poor catalytic activity observed in prior work we have evaluated the CVD conditions employed. The CVD conditions used in CNT growth from FeMoC are summarized in Fig. 9.

In the work by An et al. [16], Anderson et al. [17], and Edgar et al. [18], FeMoC is heat treated $\geq$ 700 °C before reduction of the pro-catalyst occurs by either hydrogen or the carbon precursor. Catalyst pre-treatment at 700 °C is important to note given that the sublimation point of bulk MoO_3 is $\sim$ 700 °C [41]. Prompted by this and the known quantum size effects on nanoparticles, such as increasing vapor pressure, we have investigated the volatility of FeMoC using the TGA method [42]. Details of the calculation method are given in the Supplementary Information. Plotting the linear slope of $\log(M_{sub}\sqrt{T})$ versus 1/T yields ΔH_{sub}. The results for FeMoC are shown in Fig. 10.

Figure 10b shows a distinct linear region between 650 - 750 °C with a calculated enthalpy of sublimation of 421.9 kJ/mol. This value is in good agreement with ΔH_{sub}. values for MoO_3 found in literature (387.9–450.5 kJ/mol) [43, 44]. This suggests that during the calcination step in prior work, molybdenum may have been lost due to the sublimation of volatile Mo oxides, resulting in a lower than expected composition/particle size of the eventual particle. This could possibly explain why prior work required catalyst promoters, i.e., to add additional metal making a large enough catalyst particle [45].

The catalyst promoters may also play an additional role by lowering the reduction temperature required to fully reduce the Fe-Mo components. Confirmation of this can be seen in Fig. 11, where TGA experiments of FeMoC in both 5 and 10% H_2 reduction environments are compared with FeMoC prepared with a catalyst promoter $FeCl_3$ (1:25 molar ratio FeMoC to $FeCl_3$) in 5% H_2. The results show final dTGA peaks at 697, 797, and 837 °C for 10% H_2, FeMoC + $FeCl_3$, and 5%H respectively. Considering that iron oxide is completely reduced well before its molybdenum oxide counterpart (Fig. 3), with dTGA peaks at $\sim$ 650 and $\sim$ 950 °C respectively, it is likely that Fe acts to lower the reduction temperature through the formation of Fe-Mo oxides with lower activation energies [46–48]. Gasik et al. [46] proposes that the lower activation energy arises from the tunneling of 3-d electrons of Fe into the electronic structure of MoO_3. Therefore, the additional "Fe" in the catalyst promoter aids in the "activation" of FeMoC by lowering the energy barrier needed to sufficiently reduce the pro-catalyst.

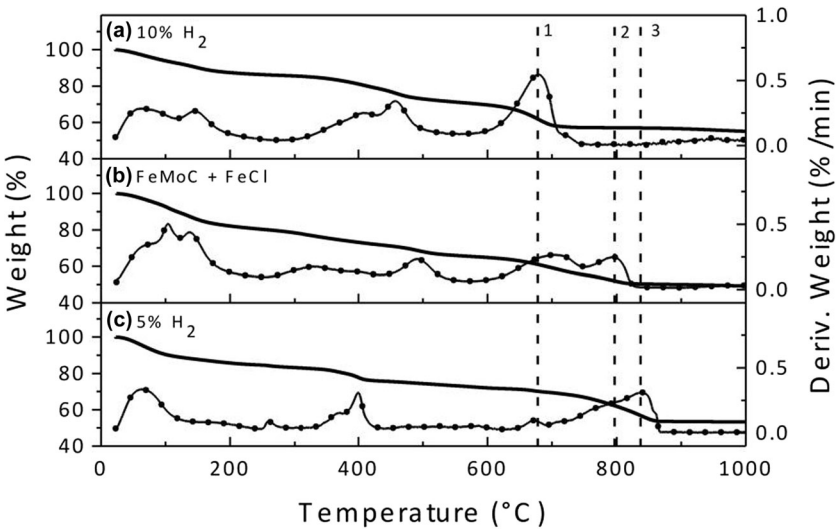

Fig. 11 TGA comparison of FeMoC reduced in 5% H_2 (**a**), FeMoC + $FeCl_3$ (1:25 molar ratio) reduced in 5% H_2 (**b**), and FeMoC reduced in 10% H_2. The weight (%) is depicted as solid lines. The deriv. weight (%/min) lines are marked with the "O" symbol. The dTGA peaks labelled correspond to 697, 797, and 837 °C, for **a**, **b**, and **c** respectively

Conclusions

Herein we have evaluated the role of CVD pre-treatment in "activating" the pro-catalyst FeMoC for CNT growth, with a central focus on elucidating why prior work required excessive temperatures (> ~ 900 °C) and catalyst promoters. We show that the mechanism for FeMoC "activation" is due to the sufficient reduction of the metal oxide components. Consideration of prior reports, including our own, of using FeMoC as a single source molecular pro-catalyst precursor [16–21] suggest that their partial failures to perform as expected were due to insufficient activation or partial sublimation of the metal oxide resulting in a smaller than necessary catalyst size [45]. These reports underline the importance of the catalyst pre-treatment step in "activating" FeMoC and related pro-catalyst for growth of CNTs.

By ensuring sufficient reduction prior to introduction of growth gasses, we demonstrate for the first time CNT growth at temperatures as low as 600 °C using FeMoC. Thus, the use of catalyst promoters likely serves two roles, (1) to replenish the number of metal atoms lost to sublimation, and (2) to reduce the reduction temperature of pro-catalyst FeMoC into an "active" catalyst. Future work will study the catalyst pre-treatment influence on the resulting phase(s) of FeMoC's Fe-Mo catalyst system; akin to the work of Li et al. [13–15] who demonstrated the reduction temperature of $Na_{15}[Na_3 \subset \{Co(H_2O)_4\}_6\{WO(H_2O)\}_3(P_2W_{12}\text{-}O_{48})_3]\cdot nH_2O$ and its impact on the resulting miller plane indices of the μ-phase W_6Co_7 resulting in their extraordinary chiral selectivity. These results provide new insights into the catalyst pre-treatment of FeMoC, opening up new possibilities for FeMoC and related pro-catalysts.

Acknowledgements Financial support for this work is provided by the NSF IRISE training program at Rice University (NSF EHR-0966303), the Robert A. Welch Foundation (C-0002), and the Welsh Government Sêr Cymru Programme. The authors declare no conflict of interest.

References

1. E. Joselevich, H. Dai, J. Liu, K. Hata, and A. H. Windle in Carbon Nanotubes, V. Jorio, and M. S. Dresselhaus (eds.), *Carbon Nanotubes* (Springer, Berlin Heidelberg, 2007), pp. 101–165.
2. R. S. Ruoff and D. C. Lorents (1995). *Carbon* **33**, 925.
3. T. W. Ebbesen, H. J. Lezec, H. Hiura, J. W. Bennett, H. F. Ghaemi, and T. Thio (1996). *Nature* **382**, 54.
4. G. Lolli, L. Zhang, L. Balzano, N. Sakulchaicharoen, Y. Tan, and D. E. Resasco (2006). *J. Phys. Chem. B* **110**, 2108.
5. A. R. Harutyunyan, G. Chen, T. M. Paronyan, E. M. Pigos, O. A. Kuznetsov, K. Hewaparakrama, S. M. Kim, D. Zakharov, E. A. Stach, and G. U. Sumanasekera (2009). *Science* **326**, 116.
6. M. He, H. Jiang, B. Liu, P. V. Fedotov, A. I. Chernov, E. D. Obraztsova, F. Cavalca, J. B. Wagner, T. W. Hansen, I. V. Anoshkin, E. A. Orbraztosva, A. V. Belkin, E. Sairanen, A. G. Nasibulin, J. Lehtonen, and E. I. Kappinen (2013). *Sci. Rep.* **3**, 1460.
7. A. G. Nasibulin, P. V. Pikhitsa, H. Jiang, and E. I. Kauppinen (2005). *Carbon* **43**, 2251.
8. C. L. Cheung, A. Kurtz, H. Park, and C. M. Lieber (2002). *J. Phys. Chem. B* **106**, 2429.
9. F. Schäffel, M. H. Rümmeli, C. Kramberger, U. Queitsch, E. Mohn, R. Kaltofen, T. Pichler, B. Büchner, B. Rellinghaus, and L. Schultz (2008). *Phys. Status Solidi A* **205**, 1382.
10. M.-F. C. Fiawoo, A.-M. Bonnot, H. Amara, C. Bichara, J. Thibault-Pénisson, and A. Loiseau (2012). *Phys. Rev. Lett.* **108**, 195503.

11. A. W. Orbaek, A. C. Owens, C. C. Crouse, C. L. Pint, R. H. Hauge, and A. R. Barron (2013). *Nanoscale* **5**, 9848.
12. A. W. Orbaek, L. Morrow, S. J. Maguire-Boyle, and A. R. Barron (2015). *J. Exp. Nanosci.* **10**, 324–349.
13. F. Yang, X. Wang, D. Zhang, J. Yang, D. Luo, Z. Xu, J. Wei, J.-Q. Wang, Z. Xu, F. Peng, X. Li, R. Li, Y. Li, M. Li, X. Bai, F. Ding, and Y. Li (2014). *Nature* **510**, 522.
14. F. Yang, X. Wang, J. Si, X. Zhao, K. Qi, C. Jin, Z. Zhang, M. Li, D. Zhang, J. Yang, Z. Zhang, Z. Xu, L.-M. Peng, X. Bai, and Y. Li (2017). *ACS Nano* **11**, 186.
15. F. Yang, X. Wang, D. Zhang, K. Qi, J. Yang, Z. Xu, M. Li, X. Zhao, and X. Li Bai (2015). *J. Am. Chem. Soc.* **137**, (27), 8688–8691.
16. L. An, J. M. Owens, L. E. McNeil, and J. Liu (2002). *J. Am. Chem. Soc.* **124**, 13688.
17. R. E. Anderson, R. Colorado, Jr., C. Crouse, D. Ogrin, B. Maruyama, M. J. Pender, C. L. Edwards, E. Whitsitt, V. C. Moore, D. Koveal, C. Lupu, M. Stewart, J. M. Tour, R. E. Smalley, and A. R. Barron (2006). *Dalton Trans.*, 3097.
18. K. Edgar and J. L. Spencer (2006). *Curr. Appl. Phys.* **6**, 419.
19. S. Jeon, C. Lee, J. Tang, J. Hone, and C. Nuckolls (2008). *Nano Res.* **1**, 427.
20. K. Goss, A. Kamra, C. Spudat, C. Meyer, P. Kögerler, and C. M. Schneider (2009). *Phys. Status Solidi B* **246**, 2494.
21. F. Peng, D. Luo, H. Sun, J. Wang, F. Yang, R. Li, J. Yang, and Y. Li (2013). *Chin. Sci. Bull.* **58**, 433.
22. E. Mora, J. M. Pigos, F. Ding, B. I. Yakobson, and A. R. Harutyunyan (2008). *J. Am. Chem. Soc.* **130**, 11840.
23. C. L. Pint, N. Nicholas, S. T. Pheasant, J. G. Duque, A. N. G. Parra-Vasquez, G. Eres, M. Pasquali, and R. H. Hauge (2008). *J. Phys. Chem. C* **112**, 14041.
24. S. K. Youn and H. G. Park (2013). *J. Phys. Chem. C* **117**, 18657.
25. A. M. Cassell, J. A. Raymakers, J. Kong, and H. Dai (1999). *J. Phys. Chem. B* **103**, 6484.
26. A. R. Harutyunyan, B. K. Pradhan, U. J. Kim, G. Chen, and P. C. Eklund (2002). *Nano Lett.* **2**, 525.
27. E. Lamouroux, P. Serp, Y. Kihn, and P. Kalck (2007). *Appl. Catal. Gen.* **323**, 162.
28. X. Wang, Q. Li, J. Xie, Z. Jin, J. Wang, Y. Li, K. Jiang, and S. Fan (2009). *Nano Lett.* **9**, 3137.
29. L. Kang, Y. Hu, H. Zhong, J. Si, S. Zhang, Q. Zhao, J. Lin, Q. Li, Z. Zhang, L. Peng, and J. Zhang (2015). *Nano Res.* **8**, 3694.
30. S. Zhang, L. Tong, Y. Hu, L. Kang, and J. Zhang (2015). *J. Am. Chem. Soc.* **137**, 8904.
31. C. A. Crouse, B. Maruyama, R. Colorado Jr., T. Back, and A. R. Barron (2008). *J. Am. Chem. Soc.* **130**, 7946.
32. A. W. Orbaek, A. C. Owens, and A. R. Barron (2011). *Nano Lett.* **11**, 2871.
33. S. Sun, H. Zeng, D. B. Robinson, S. Raoux, P. M. Rice, S. X. Wang, and G. Li (2004). *J. Am. Chem. Soc.* **126**, 273.
34. J. C. Park and H. Song (2007). *Chem. Mater.* **19**, 2706.
35. A. W. Orbaek, N. Aggarwal, and A. R. Barron (2013). *J. Mater. Chem. A* **1**, 14122.
36. H. Yoshida, T. Shimizu, T. Uchiyama, H. Kohno, Y. Homma, and S. Takeda (2009). *Nano Lett.* **9**, 3810.
37. M. S. Dresselhaus, G. Dresselhaus, R. Saito, and A. Jorio (2005). *Phys. Rep.* **409**, 47.
38. G. D. Nessim, A. J. Hart, J. S. Kim, D. Acquaviva, J. Oh, C. D. Morgan, M. Seita, J. S. Leib, and C. V. Thompson (2008). *Nano Lett.* **8**, 3587.
39. G. Chen, R. C. Davis, D. N. Futaba, S. Sakurai, K. Kobashi, M. Yumura, and K. Hata (2016). *Nanoscale* **8**, 162.
40. H. Wang, Y. Yuan, L. Wei, K. Goh, D. Yu, and Y. Chen (2015). *Carbon* **81**, 1.
41. C. K. Gupta *Extractive Metallurgy of Molybdenum* (CRC Press, Boca Raton, 1992).
42. E. G. Gillan, S. G. Bott, and A. R. Barron (1997). *Chem. Mater.* **9**, 796.
43. L. Brewer *Molybdenum: Physico-Chemical Properties of Its Compounds and Alloys* (Unipub, New York, 1980), pp. 1–714.
44. M. S. Samant, A. S. Kerkar, S. R. Bharadwaj, and S. R. Dharwadkar (1992). *J. Alloys Compd.* **187**, 373.
45. F. Ding, A. Rosén, and K. Bolton (2004). *J. Chem. Phys.* **121**, 2775.
46. M. M. Gasik and P. N. Ostrik (2014). *J. Therm. Anal.* **40**, 313.
47. S. Qin, C. Zhang, J. Xu, Y. Yang, H. Xiang, and Y. Li (2011). *Appl. Catal. Gen.* **392**, 118.
48. S. S. Al-Shihry and S. A. Halawy (1996). *J. Mol. Catal. Chem.* **113**, 479.